euspen's 26th International Conference & Exhibition, Krakow, PL, June 2026
www.euspen.eu

Internal Quality Optimisation of Material Extrusion Additive Manufacturing via Computer Vision-Enhanced Layerwise Surface Topography Measurement

Kexin Yin*[1], Yuchu Qin[1], Shan Lou[1], Paul Scott[1], Xiangqian Jiang [1]

[1] *EPSRC Future Advanced Metrology Hub for Sustainable Manufacturing, University of Huddersfield, Huddersfield, United Kingdom, HD1 3DH*

Kexin.yin@hud.ac.uk

Abstract
In-situ quality assurance has become a critical industrial imperative for material extrusion additive manufacturing to guarantee the overall internal quality. However, existing real-time monitoring techniques largely fail to dynamically bridge accessible 2D surface metrology with complex 3D internal structural integrity during the continuous fabrication process. This research proposes a novel closed-loop optimisation framework that integrates a novel ordinal CNN for layerwise Sa and Sdr prediction related to porosity, achieving a Sa prediction RMSE of 2.88(±0.23) and a Sdr prediction RMSE of 4.95(±0.81), and a Gaussian Process Regression controller to dynamically regulate extrusion temperature and velocity against cumulative thermal drift. The framework's overall closed-loop efficacy was verified through physical cross-sectional morphological analyses and an implicit neural network-driven surface simulation, showing autonomous disturbance rejection and self-healing, reducing internal porosity from over 2.0% to below 0.7%.
Keywords
Computer Vision, Artificial Intelligence, In-process Measurement, Optimisation,Additive Manufacturing

1. Background

Despite material extrusion additive manufacturing's widespread application across aerospace, automotive, and biomedical sectors, ensuring overall consistent part quality remains a pressing concern. The fundamental layer-by-layer fabrication of AM leads to defects from heat and conjunctions. Because these defects are often hidden within the structure, the lack of robust, internal quality monitoring remains a major pain point, limiting AM's full adoption in high-stakes manufacturing.

To mitigate these inherent defects, extensive research over the past decade has predominantly focused on the offline optimisation of process parameters. For instance, Rayegani and Onwubolu [1] utilised the group method for data handling to successfully predict and optimise the complex relationship between printing parameters and tensile strength. Addressing surface quality, Abouzaid et al. [2] modelled how temperature variations critically impact the mechanical performance, roughness, and porosity of resulting composite products. While these offline optimisation strategies have laid a solid foundation, they operate under the assumption of static printing conditions and fail to account for dynamic disturbance.

To overcome the limitations of static offline settings, online detection technologies have progressed rapidly in recent years. Kandananond [3] used artificial neural networks and the Box–Behnken method to improve the prediction accuracy of surface roughness in FFF parts based on process parameters. Similarly, Muhammad et al. [4] proposed a deep neural network for predicting Sa roughness in LPBF-built aluminium alloys, achieving high accuracy compared with experimental measurements. In addition, Toorandaz et al. [5] integrated in-situ photodiode sensing with machine learning models such as Random Forest, successfully predicting surface roughness in real time. However, merely identifying defects as they occur is insufficient if the manufacturing system cannot autonomously correct them.

A critical gap persists in effectively bridging the transition from passive online monitoring to active, closed-loop parameter optimisation. To address it, this study proposes a novel closed-loop control framework that integrates real-time surface quality monitoring with a dynamic parameter optimisation algorithm. By establishing a direct correlation between 2D surface morphology and 3D internal defects, this research aims to actively suppress porosity during the printing process.

The primary contributions of this paper are as follows. (1) the development of a rapid, non-destructive online detection method for surface roughness utilizing industrial machine vision; (2) the implementation of a time-varying optimisation GPR model for macroscopic feedforward prediction and a P control strategy for microscopic feedback adjustment; and (3) the proposition of a process-driven digital twin model based on virtual stacking, which effectively maps real-time surface parameters to internal porosity evaluation.

2. Methodology

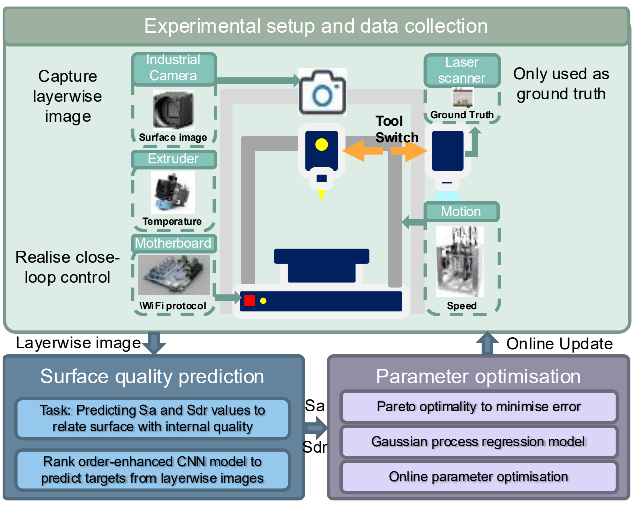

Figure 1. Overview of the workflow

As illustrated in Figure 1, the closed-loop framework is implemented on a Wi-Fi-enabled, 3-axis FDM printer within a stably illuminated chamber. The continuous control cycle initiates immediately post-deposition: a mounted XIMEA camera captures a high-resolution surface image, which is processed by a CNN model to predict surface roughness (Sa) and developed interfacial area ratio (Sdr). Subsequently, a Gaussian Process Regression (GPR) model determines the optimal extrusion temperature (190°C–240°C) and printing speed (40mm/s-150mm/s) for the next layer, actively compensating for cumulative thermal drift while maintaining efficiency. These optimised parameters instantly update the local G-code via Wi-Fi for the subsequent execution. While a scanCONTROL laser scanner was employed exclusively during model development to establish ground-truth point clouds, it was omitted during actual fabrication. Although porosity may be less problematic in large FDM components due to non-solid interiors, it is meaningful to conduct such cheap experiments to prove the feasibility and later transfer the knowledge to metal additive manufacturing. The dataset contains 3130 samples out of 21 30mm height blocks, with 2190 for training and 940 for testing.

2.1. Layerwise surface quality prediction model

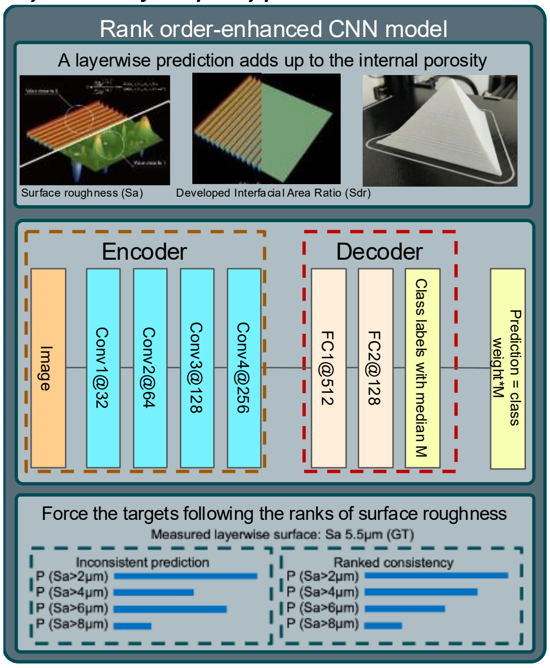

Figure 2. Rank-ordered layerwise prediction model

As shown in Figure 2, Sa and Sdr are selected as the core indicators of layerwise surface quality and are further related to interior porosity. Sa quantifies the average deviation of the surface from a mean plane, providing a measure of surface smoothness. In the context of 3D printing, the smoothness of each layer directly influences the subsequent deposition process. Sdr measures the percentage increase in actual surface area relative to an ideal reference plane and therefore reflects the structural complexity generated by peaks and valleys that form along the extrusion path. In extrusion-based printing, anisotropic surface textures naturally appear due to line-by-line deposition at alternating angles. When Sdr is high, meaning the peaks are tall and the valleys are deep, insufficient material flow or suboptimal filling may leave unfilled gaps within the valleys, forming pores [6]. The accumulation of such voids across multiple layers increases the internal porosity of the component, which directly affects the mechanical and functional performance of the final part.

The proposed layerwise surface quality prediction network adopts a lightweight CNN architecture rather than a deep SOTA model due to limited samples with simple stripe-like textures to avoid overfitting. The classification decoder branch performs coarse classification of each printing layer into six ordered categories [7] defined by K-means clustering of Sa values. The model learns a sequence of binary decisions of the form "Is the surface quality at least Level k?". Each decision is made by a shared-weight structure that reuses the same feature representation $a_{1...n}$ and applies a series of linear classifiers W1...n to predict the probability y>k. The predicted class is determined by the highest k for which the answer remains true. The final layers of the classification branch are designed as shown in Figure 3. The final numerical result is obtained by the sum of the products of its classification probability and the statistical median of the corresponding category. The loss function CORAL [8] constrains the predicted logits so that class decision boundaries remain monotonic; that is, the logit corresponding to level k+1 must not exceed that of level k, defined as:

$$L_{cls} = -\sum_{i=1}^{N}\sum_{k=1}^{K-1}\left(t_{i,k}\cdot\log\left(\sigma(g_{i,k})\right) + (1-t_{i,k})\cdot\log\left(1-\sigma(g_{i,k})\right)\right) \tag{1}$$

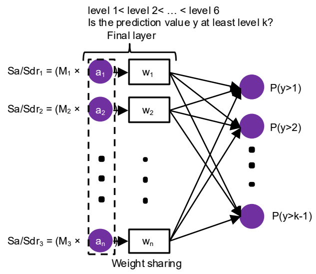

Figure 3. The final layers of the Rank-ordered CNN

2.2. Optimisation Strategy

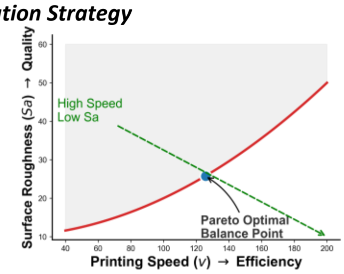

Figure 4. Trade-off explanation between quality and efficiency

The primary objective of the proposed online optimisation model is to accurately control the Sa and developed interfacial area ratio Sdr of the current printing layer by dynamically adjusting the extrusion temperature and printing speed. To achieve this, a comprehensive multi-objective target function, denoted as $J(X_{n+1})$, is formulated for subsequent layers, evaluated by minimising the squared error.

A fundamental challenge addressed by the optimisation is the inherent physical trade-off between manufacturing efficiency and surface quality. As shown in Figure 4, increasing the printing speed v to improve efficiency tends to a higher Sa value. To prevent the algorithm from selecting impractically slow speeds in pursuit of perfect smoothness, an efficiency dependency term, 1/v, is integrated into the target function.

In addition to efficiency, the optimisation model must explicitly compensate for the non-linear thermal accumulation that progressively occurs across successive printed layers. As shown in the thermal drift comparison chart, the actual thermal state of the printed part tends to saturate over time, diverging significantly from a theoretical linear hypothesis. To counteract this phenomenon, a temporally dependent drift compensation function, Φ(n), is embedded.

$$J(X_{n+1}) = \omega_1\cdot\left(R_{pred} - R_{target}\right)^2 + \omega_2\cdot\frac{1}{v} + \Phi(n) \tag{2}$$

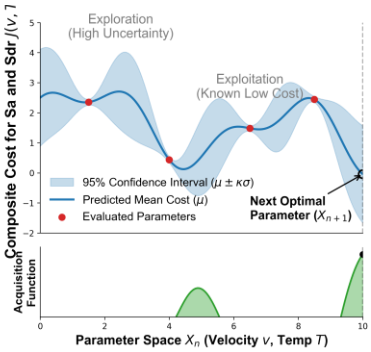

Figure 5. GPR model theorem

To solve the multi-objective target function, a GPR [10] model is employed as the primary optimisation engine. Unlike traditional deterministic algorithms, GPR utilises a non-parametric Bayesian inference approach to output both a predicted mean μ and a 95% confidence interval μ ± σ. This ability to explicitly quantify predictive uncertainty is essential for the FDM process, where layer-wise thermal fluctuations introduce inevitable environmental noise. Guided by these probabilistic outputs, an Upper Confidence Bound (UCB) acquisition function is applied to determine the next optimal parameter, denoted as x_{n+1}. The UCB mathematically drives the search process by strictly balancing 'exploitation' of regions with a known low cost against the 'exploration' of unmapped parameters exhibiting high uncertainty.

$$x_{n+1} = \arg\min_{x} \mu(x) + \kappa \cdot \sigma(x) \tag{3}$$

The underlying smoothness of this GPR model is governed by the Squared Exponential (SE) kernel. This specific kernel is selected because its infinitely differentiable nature aligns perfectly with the gradual, continuous thermal transitions inherent to 3D printing. Modulated by a length scale l and variance σ^2, the SE kernel operates on the physical assumption that operational parameters situated closer together in the input space share maximum correlation, shown as:

$$k(x, x') = \sigma_f^2 \exp\left(-\frac{|x - x'|^2}{2l^2}\right) \tag{4}$$

To actualise dynamic, layer-by-layer execution, a Proportional (P) feedback controller is integrated into the final stage of the online parameter optimisation. While the GPR model already mathematically anticipates temporal thermal drift, the addition of P-control constitutes a complementary necessity rather than a repetition. The GPR function remains inherently vulnerable to unmodelled stochastic disturbances, such as material or ambient temperature shifts. Therefore, the P-control, formulated as $u_{n+1} = f(X_n) + K_p \times$ error, acts as a microscopic corrective mechanism that strictly compensates for immediate, real-time residual errors.

2.3. Process-driven Surface Generator

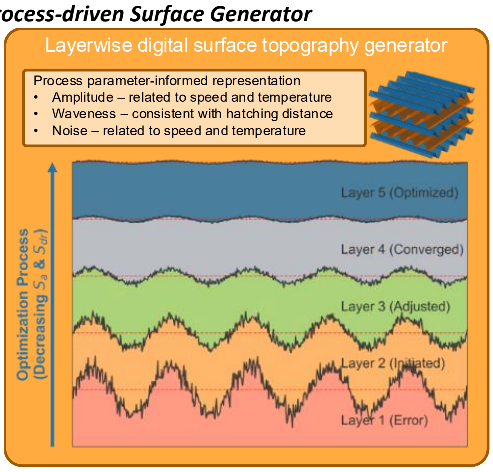

Figure 6. The workflow of the Virtual Metrology

As shown in Figure 6, The digital top surface generation is governed by an MLP designed for implicit morphological prediction. To accurately capture the physical layer-to-layer geometric inheritance the network takes a four-dimensional input vector: the current printing speed v and temperature T, and the preceding layer's quality (Sa_{n-1} and Sdr_{n-1}). The model predicts the topographical amplitude (A) and stochastic noise (σ). Subsequently, these predicted modifiers are injected into the parametric surface generator to digitally reconstruct the 3D point cloud of the current layer. Finally, the simulated Sa_n and Sdr_n are calculated from this generated point cloud for verification. This virtual surface generation is not conducted as a series of isolated, independent single-layer simulations, but rather as a continuously correlated progression with the online optimisation algorithm feedback to improve the v and T. The cross-hatching strategy is used, where each subsequent layer is deposited perpendicularly to the current one.

3. Result

3.1. Layerwise Prediction Performance

From Table 1, the classification-based approach (Base2 + CE) demonstrates a measurable improvement over plain direct regression (Base1). This confirms that initially mapping samples into discrete, ordered quality bands before converting them to numeric values presents an easier learning objective than full-range continuous regression. Furthermore, integrating the CORAL loss function into the classification framework yields the most significant enhancements. Our configuration achieves the highest overall accuracy with the largest std reduction, proving CORAL-enhanced model is not only more accurate but also robust to random initialisation or varying dataset splits.

Table 1 Result comparison of layerwise quality prediction

Model Configuration	Avg RMSE for Sa (Std)	Avg MAE for Sa (Std)	Avg RMSE for Sdr (Std)	Avg MAE for Sdr (Std)
Direct regression [9]	3.71 (0.76)	2.5 (0.23)	6.09 (1.16)	3.84 (0.50)
Classification to value [7] + CE	3.44 (0.65)	2.3 (0.15)	5.90 (1.18)	3.78 (0.41)
Ours	2.88 (0.23)	1.81 (0.05)	4.95 (0.81)	3.05 (0.24)

3.2. Optimisation Model Performance

Table 2 quantitatively evaluates the dynamic performance and stability of the proposed online optimisation strategy. To assess the fundamental accuracy of the surrogate model, Predictive R^2 and Prediction Interval Coverage Probability (PICP) are utilised. The proposed method demonstrates superior prediction accuracy and highly reliable uncertainty quantification compared to the standard GPR model without thermal considerations. Further, the long-term robustness against thermal accumulation is strictly evaluated using the Steady-State Error and the Integral Time Absolute Error (ITAE) score, a metric that heavily penalises uncorrected drifting errors as the printing time increases. While the fixed-parameter baseline completely fails to converge due to severe thermal drift, the proposed method drastically reduces the steady-state error to just 0.21 μm and the ITAE score to 85.3.

Table 2 Result comparison of optimisation modelling

Optimisation Strategy	Predictive R2	Predictive PICP (%)	Steady-State Error (μm)	ITAE Score
Baseline (linear Params) [11]	-	-	3.42 (Drifting)	1450.2
GPR (Without thermal factor) [10]	0.85	82.10%	1.15	420.5
Ours	0.94	94.80%	0.21	85.3

3.3. Internal Quality Verification and Virtual Metrology Results

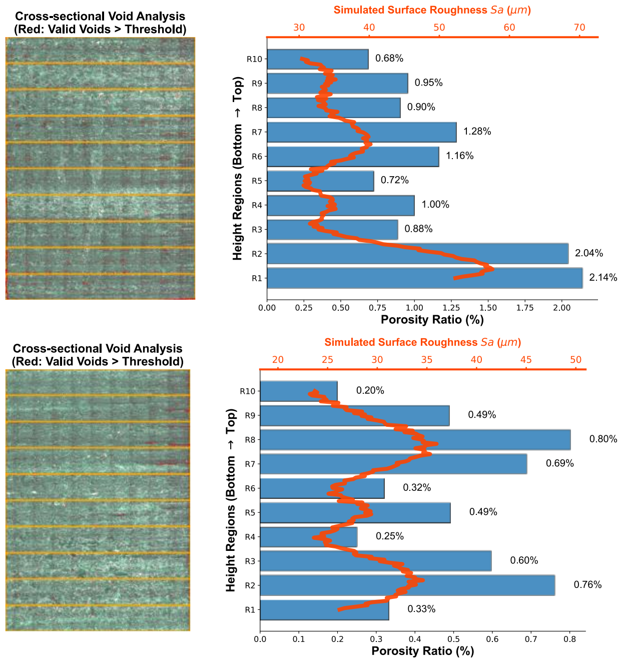

Figure 7. Porosity analysis of the cross-section with dynamically simulated surface quality results – poor start (up) and vibration (down)

To quantitatively evaluate the layer-wise efficacy of the proposed closed-loop framework, two morphological cases were performed on the optical cross-sections of 30 mm height specimens cut along their diagonal [12], which are uniformly segmented into 10 rectangular regions. Following image binarisation and area thresholding to exclusively isolate valid macroscopic voids marked in red, the localised porosity ratio for each region was calculated to track the bottom-to-top evolution of internal structural quality.

As shown in Figure 7, in the first case, a print initiated with severely suboptimal parameters (190°C, 150 mm/s) exhibited significant foundational defects, marked by a 2.14% porosity in R1. However, the surface quality prediction and GPR models iteratively corrected these errors, steadily suppressing defect formation and driving the porosity down to a negligible 0.68% by R10. In the second case, a stable print commencing with optimal parameters (yielding 0.33% initial porosity) was deliberately subjected to sudden temperature and speed disturbances. Although these anomalies caused temporary porosity spikes (peaking at 0.80% around R8), the online system immediately detected the surface degradation and enforced compensatory parameters, rapidly recovering the internal density to a 0.20% porosity by the final layer. Together, these results demonstrate the system's exceptional capability to both autonomously rescue a failing print and dynamically self-heal against unpredictable manufacturing deviations.

The digital top surface generation was governed by empirical mappings from the previous layer quality and current control parameters. As depicted in the simulation results, the digital trajectories closely mirror the physical cross-sections. As shown in orange in Figure 7, in Case 1, the model demonstrates rapid algorithmic convergence, aggressively reducing an initially severe roughness (Sa≈50μm) down to a stable optimum (Sa≈20μm). Conversely, Case 2 clearly illustrates the framework's robust disturbance rejection, where two artificially induced spikes in roughness (Sa≈40μm) are swiftly detected and autonomously suppressed back to the baseline, confirming the optimisation algorithm's stability.

4. *Conclusion and Future Work*

To address the challenge of in-situ quality assurance in FDM 3D printing, this research proposes a closed-loop optimisation framework that bridges 2D surface metrology with 3D internal structural integrity. The system integrates a CORAL-enhanced CNN, achieving a Sa prediction RMSE of 2.88(±0.23) and a Sdr prediction RMSE of 4.95(±0.81), by preserving ordinal data relationships, and a GPR controller optimise extrusion temperature and velocity against cumulative thermal drift dynamically. The framework's efficacy was strictly verified through physical cross-sectional morphological analysis and an implicit neural network-driven virtual stacking simulation. The framework's efficacy was verified through physical cross-sectional morphological analysis and an implicit neural network-driven virtual stacking simulation. Results demonstrated the system's capability in autonomous self-healing and disturbance rejection, suppressing inter-layer defects within 15 layers and reducing internal porosity from over 2.0% to below 0.7%.

Future research will focus on non-destructive X-ray Computed Tomography (XCT) verification and comprehensive inter-layer coupling simulation towards a digital twin.

Acknowledgement

The authors gratefully acknowledge the support of EPSRC funding EP/P006930/1, EP/S000453/1. Thanks for the help from Darragh Broadbent, Weidong Liu, and other colleagues.

References

[1] F. Rayegani and G. C. Onwubolu, The International Journal of Advanced Manufacturing Technology, vol. 73, no. 1–4, pp. 509–519, Apr. 2014, doi: https://doi.org/10.1007/s00170-014-5835-2.

[2] K. Abouzaid, D. Bassir, S. Guessasma, and H. Yue, Mechanics of Composite Materials, vol. 56, no. 6, pp. 805–816, Jan. 2021, doi: https://doi.org/10.1007/s11029-021-09925-6.

[3] K. Kandananond, International Journal of Metrology and Quality Engineering, vol. 12, pp. 17–17, Jan. 2021, doi: https://doi.org/10.1051/ijmqe/2021014.

[4] W. Muhammad, J. Kang, O. Ibragimova, and Kaan Inal, Welding in the World, vol. 67, no. 4, pp. 897–921, Dec. 2022, doi: https://doi.org/10.1007/s40194-022-01445-8.

[5] S. Toorandaz, K. Taherkhani, F. Liravi, and E. Toyserkani, "A novel machine learning-based approach for in-situ surface roughness prediction in laser powder-bed fusion," Additive Manufacturing, vol. 91, p. 104354, Jul. 2024, doi: https://doi.org/10.1016/j.addma.2024.104354.

[6] L. Hu et al., Virtual and Physical Prototyping, Aug. 2025, doi: https://doi.org/10.1080/17452759.2025.2541829.

[7] A. Valikhani, A. Jaberi Jahromi, S. Pouyanfar, I. M. Mantawy, and A. Azizinamini, "Machine learning and image processing approaches for estimating concrete surface roughness using basic cameras," Computer-Aided Civil and Infrastructure Engineering, Aug. 2020, doi: https://doi.org/10.1111/mice.12605.

[8] W. Cao, V. Mirjalili, and S. Raschka, "Rank consistent ordinal regression for neural networks with application to age estimation," Pattern Recognition Letters, vol. 140, pp. 325–331, Dec. 2020, doi: https://doi.org/10.1016/j.patrec.2020.11.008.

[9] F. Jáñez-Martino, E. Fidalgo, S. Martínez-Pellitero, S. Giganto, and E. Alegre, International Journal of Computer Integrated Manufacturing, pp. 1–12, Apr. 2025, doi: https://doi.org/10.1080/0951192x.2025.2498081.

[10] S. H. Lee, Metals, vol. 10, no. 4, p. 461, Apr. 2020, doi: https://doi.org/10.3390/met10040461.

[11] R. Anitha, S. Arunachalam, and P. Radhakrishnan, "Critical parameters influencing the quality of prototypes in fused deposition modelling," Journal of Materials Processing Technology, vol. 118, no. 1–3, pp. 385–388, Dec. 2001, doi: https://doi.org/10.1016/s0924-0136(01)00980-3.

[12] Y. Tao et al., Journal of Materials Research and Technology, vol. 15, pp. 4860–4879, Nov. 2021, doi: https://doi.org/10.1016/j.jmrt.2021.10.108.